An investigation of the appearance of lustering on HMPE fiber ropes

Cédric Bain, Yann Marco, Peter Davies, G. Bles, Thibault Reinhart, Pierre-Antoine Albouy

An investigation of the appearance of lustering on HMPE fiber ropes

Cédric BAIN [1, 2, 3], Yann MARCO [1], Peter DAVIES [2], Guilhem BLES [1], Thibault REINHART [3], Pierre-Antoine ALBOUY [4]

[1] ENSTA Bretagne, Institut de Recherche Dupuy de Lôme IRDL-UMR CNRS 6027, Brest, France

[2] IFREMER Centre Bretagne, Marine Structures Laboratory, Plouzané, France

[3] INO-ROPE, Concarneau, France

[4] Laboratoire de Physique des Solides, CNRS, Université Paris-Sud, Université Paris-Saclay, 91405, Orsay, France

Abstract

The low friction coefficient of HMPE fibers may be a disadvantage for some applications such as winches but it can also be used to develop new technology. Recently this specific property was used in the design of innovative pulleys for sailboats. The contact is then between a low friction metallic ring and a HMPE fiber rope loop. During service, a specific phenomenon appears at the contact area on the HMPE fibers called lustering due to its visual aspect. It is also observed in eye splice contact zones during tensile testing. In the present work, an investigation was made to understand and explain the appearance of the lustering of the fibers. Based on examination of different hypotheses, mechanical tests and a range of microstructural observations, the conclusion is that the appearance of the lustering phenomenon is the result of compaction of the filaments of the HMPE rope loop.

Keywords: HMPE, rope, compaction, lustering, fiber, microstructure

Introduction

Understanding the internal deformation mechanisms of fibrous materials during complex mechanical loading is one of the key elements in predicting the mechanical behavior of ropes. High molecular weight polyethylene fibers are increasingly used in both the marine and ballistic protection sectors thanks to their high stiffness and strength, environmental resistance and light weight (Vlasblom, 2018). Another characteristic of HMPE fibers is their low friction coefficient. Various studies have been performed on HMPE friction, in particular to try to improve the adhesion properties of HMPE (Jin et al., 2016), but this low friction behavior has also been used to create novel lightweight textile pulleys, made of a low friction metallic ring and a HMPE rope loop (Figure 1.a.). The contact between these two components creates a complex mechanical loading: both tension and compression are present, together with temperature increases due to friction. Experience with these pulleys has revealed an interesting polishing phenomenon on the contact surface known as "lustering". The latter results in a decrease in the friction of the HMPE fibers, and can also be observed in the contact region between the eye splices of tensile rope samples and steel loading pins. Figure 1.b. shows how the load needed to rotate the textile pulley changes with the number of cycles. The strength decrease is correlated to a friction coefficient decrease and the appearance of the lustering phenomenon (Bain, 2020).

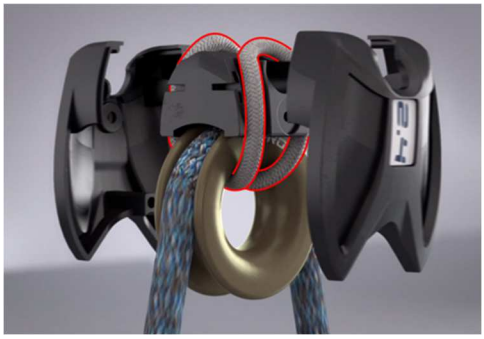

Figure 1.a. Lightweight textile pulleys, made of a low friction ring and a HMPE rope loop

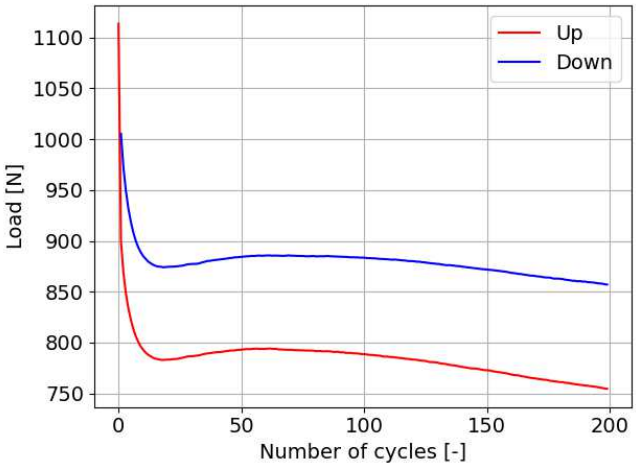

Figure 1.b. Change in the load needed to rotate a textile pulley versus the number of cycles under an 8kN static load (Bain, 2020)

The purpose of this study is to understand the appearance of this phenomenon. The lustering can be characterized by three aspects: darkening, a good optical reflection of the contact area, and a fiber cohesion that makes the fibers look like a homogenous polymer material.

Preliminary observations were made on this phenomenon. First it seems to be reversible; by applying a multi-directional bending of the contact area, the lustering disappears and individual fibers re-appear. Also, SEM (Scanning Electron Microscopy) observations were made on lustered fibers. The SEM images show no sign of abrasion and a very low surface roughness for the lustered area. It is almost impossible to distinguish the individual fibers in this region.

Based on these first observations, a literature review of previous studies was performed. Caldwell et al. (2005) studied the orientation of fibers in wool fiber assemblies. Wool fibers are made of a multitude of fiber scales from nanometer to around 20 micrometers diameter for the final fiber. Through tomography observations, Caldwell et al. showed different wool fiber arrangements with respect to the neutral axis. A specific fiber arrangement was observed in which wool fibers are compacted in their section in a prismatic pattern and the wool filaments are parallel to one another. This kind of arrangement was also observed by Bunsell (2018) for Dyneema™ SK76 fibers. For ballistic applications, Golovin & Phoenix (2016); McDaniel et al. (2017) and Sockalingam et al. (2017) studied the effect of transverse compression on HMPE filament behavior and on its meso- and nano-structure. McDaniel et al. (2017) observed a misalignment and a lack of compaction of the fibrils which composed the HMPE filaments after a transverse compression. Also, Golovin & Phoenix (2016) showed a drop in tensile strength of the HMPE filament after a transverse compression caused by a decrease in crystallinity from 95 to 80 %, and a reduction in crystallite size by about a factor of two. These conclusions have been supported with Differential Scanning Calorimetry (DSC) analysis and birefringence images. Golovin & Phoenix (2016) observed that HMPE filaments become optically transparent when they are thin enough. These previous studies on transverse compression were made at ambient temperature. Some other studies focused on the microstructure of HMPE (Dyneema™) fibers under the influence of the temperature and stretching. Tian et al. (2015) showed through wide-angle X-ray scattering (WAXS) analysis and Raman spectroscopy that a macroscopic deformation induced microstructural changes in HDPE films: a lamellar structure could transform into micro-fibrils with stress-induced melting and crystallization mechanisms (Jiang et al., 2007; Tang et al., 2007). Also, Tian et al. (2015) observed that a high temperature helps the formation of fibrillar crystals. The transition between lamellar and "shish-kebab" states happens smoothly in SAXS observations. Forster et al. (2015) demonstrated that HMPE fibers exposed to high temperatures may undergo shrinkage and loss of orientation. McDaniel et al. (2015) compared several types of fibers with a high-resolution microscope and WAXS observations. That study showed a modification in the microstructure of HMPE fibers during the stretching process. Finally, through WAXS observations and Raman spectroscopy, Litvinov et al. (2011) concluded that an increase of the fiber deformation during the stretching process leads to an increase in the degree of crystallinity and an increase in the fiber modulus. Also, a specific process of hot compaction to create HMPE fibers and polypropylene (PP) fiber composite was studied by Hine et al. (1993), Olley et

al. (1993), Kabeel et al. (1994), El-Maaty et al. (1996), Yan et al. (1997) and Morye et al. (1999). A specific fiber arrangement has been observed by Olley et al. (1993), Kabeel et al. (1994), Yan et al. (1997) for HMPE fibers and by El-Maaty et al. (1996) for PP fibers. This hot compaction process produces a homogeneous material with similar original fiber properties. An optimal set of parameters (temperature, pression, time) allows a portion of fibers to melt. On cooling, the molten material recrystallizes to form a "glue" to bind the structure together. The thermomechanical loading is similar to that of the HMPE rope loop in the contact area. For the HMPE rope loop, fibers are also stretched. The temperature for the hot compaction process is near the melting temperature of HMPE fibers, which is higher than for the maximal service temperature of the pulley or for a hot bedding-in. Kabeel et al. (1994) explained that a raised temperature induces softness, so that the application of pressure compresses the fibers into a near-solid mass. He observed that this produces hexagonal arrays. Olley et al. (1993) showed that at 138 °C, melting (and recrystallization) only occurs in regions where molten polymer is not constrained to remain oriented.

Based on the first observations made and these previous studies on the microstructure of fibers, four hypotheses can be made to explain the appearance of "lustering" on the contact surface of the HMPE rope loop:

1. Coating migration to the outer surface of the HMPE loop
2. Fiber compaction in the transverse direction
3. Plasticity in HMPE fibers.
4. Microstructure modification due the complex thermomechanical loading undergone by the HMPE loop

In order to test these hypotheses one by one, various observations and analyses have been made. Based on the results, the discussion will provide conclusions about the validity of each of these hypotheses.

1. Material and Methods

1.1. Material

Different grades of Dyneema™ HMPE fibers were used during the study: Dyneema™ SK99 and SK78. First observations were made on a Dyneema™ SK78 braided rope with a 500kN break load. Other observations were made on Dyneema™ SK99 fibers with and without coating. The samples were provided by the Lancelin Corderie (Ernée, France).

1.2. Samples and Experimental Devices

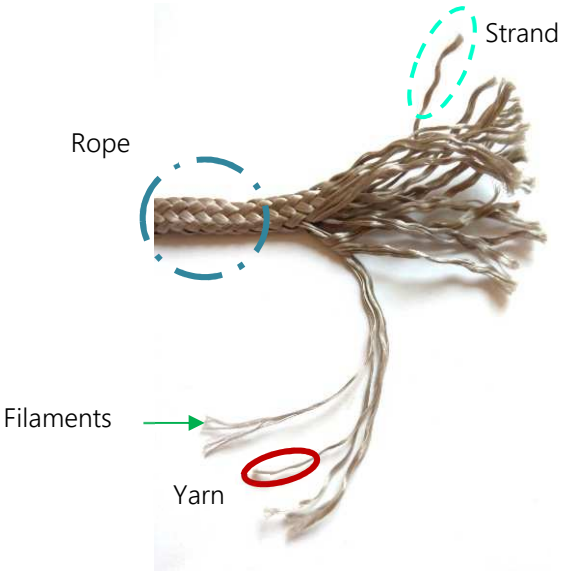

Figure 2.a. The different scales of the Dyneema™ SK99 braided rope of the study with a 4mm diameter, coating and a Mean Breaking Load (MBL) of 14.7kN.

Figure 2.b. The different scales of the Dyneema™ SK78 braided rope with a diameter of 22mm, coating and a MBL of 500kN (Sample K in red)

The braided ropes have different component scales, from the largest to the smallest as follows: the braided rope, the strand, the yarn and the filament (Figure 2.a). For bigger ropes, some extra scales can be added such as sub-strands and rope yarns. The fibers without coating are white in contrast to the coated ones which are grey. The composition of the coating is proprietary and confidential.

Different kinds of samples were employed in order to investigate the four hypotheses made to explain the appearance of the "lustering" phenomenon. These are listed below in Table 1:

Sample	Type	Scale (see Figure 2)	Fiber state (see Figure 3)	Loading (see Figure 4)
A	SK99	Part Textile axis	coated, lustered and not lustered	Dynamic loading
B	SK99	Part Textile axis	uncoated, lustered and not lustered	Dynamic loading
C	SK99	Strand from 4mm diameter rope	uncoated	None
D	SK99	Strand from 4mm diameter rope	coated	None

E	SK99	Strand from a textile axis	coated, lustered	Dynamic loading of 2kN
F	SK99	Strand from a textile axis	coated, lustered	Quasi-static loading of 8kN
G	SK99	Strand from a textile axis	coated, not lustered	Dynamic loading of 2kN
H	SK99	Strand from 4mm diameter rope	coated	bedding-in process at ambient temperature
I	SK99	Strand from 4mm diameter rope	coated	bedding-in process at 100°C
J	SK78	4mm diameter rope	coated, not lustered	None
K	SK78	Yarn from 22mm diameter rope	coated, lustered	Hot bedding-in
L	SK78	Yarn from 22mm diameter rope	not lustered	Hot bedding-in and de-lustering process

Table 1. Samples examined

131

132 The details of the samples are described according to the type of observation.

133 The difference between the fibers coated and uncoated can be seen on Figure 3.a and Figure 3.b.

134 Uncoated HMPE fibers are white while coated HMPE fibers for this study are gray.

135

Figure 3. a. Coated HMPE fiber rope, 4mm diameter

Figure 3. b. Uncoated HMPE fiber rope, 4mm diameter

136

137 Experimentally, two different methods are used to rotate the pulley: dynamic loading and quasi-static

138 lading. For both loading a specific device is needed. Figure 4.a and Figure 4.b show the different loadings.

139

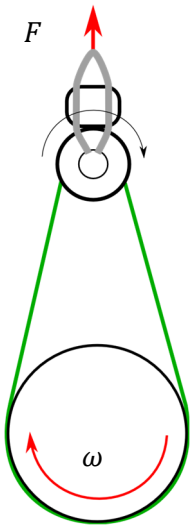

Figure 4.a. Dynamic loading

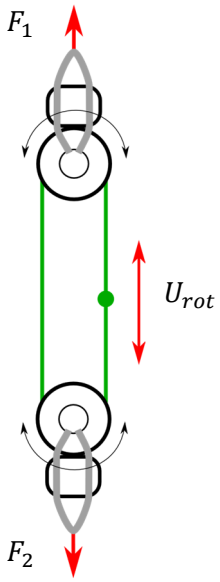

Figure 4.b Quasi-static loading

In the case of dynamic loading, the pulley is constantly rotating with an electric motor ($W = 51rpm$ which leads to a sliding speed around 0.2m/s) until the pulley reaches a stable temperature. The force F is applied by a tensile test machine.

For quasi-static loading, the force F is applied through a specially designed frame and a tensile test machine applies the displacement U_{rot} . The pulley is alternatively rotating with a displacement speed of 20mm/min. The number of cycles was chosen arbitrarily, and fixed here at 100 cycles. The pressure results from the contact area, the geometry of the pulley and the global applied tension. A pressure of 71 MPa was calculated (based on measurements by Bain (2020)).

The bedding-in process at 100°C for sample I corresponds to one load/unload cycle at 20% stretching at 100°C of a 4mm diameter rope. And for the bedding-in process at ambient temperature for sample H it corresponds to one load/unload cycle at 3% stretching at ambient temperature of a 4mm diameter rope.

A de-lustering protocol was applied to lustered sub-strands. The protocol is described on Figure 5. It consists of unpacking and tousling fibers by bending the lustered sub-strands in several directions.

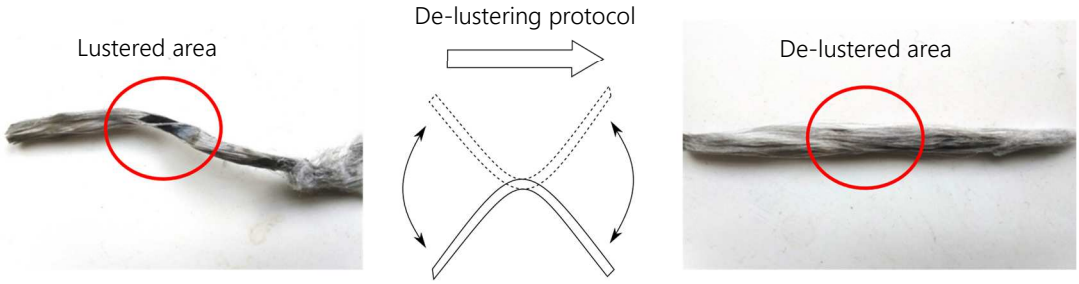

Figure 5. De-lustering protocol

1.2.1. Scanning Electron Microscope (SEM) samples

The zone of interest extracted from the rope for SEM depends on whether it is a single fiber, a strand or an entire braided rope section. For this study strands, braided rope sections and parts of the textile axis of the pulley were observed. In order to have the best image, the electron beam gun of the SEM has to be relatively close to the samples. For this reason, in the case of the textile axis, the sample has the geometry shown in Figure 6. The SEM used for these observations is a JEOL JSM-IT300 at ENSTA Bretagne.

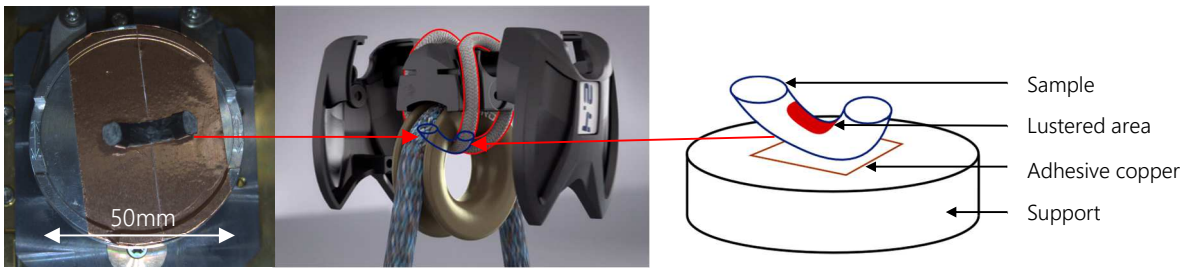

Figure 6. Sample A: Part of 4mm diameter textile axis with lustered area

The other samples are placed on a support as shown in Figure 7 (top view).

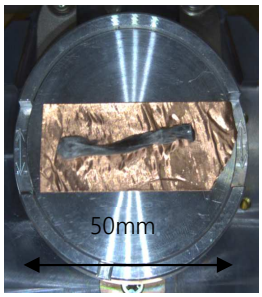

Figure 7. Sample K (see Table 1 and Figure 2b) before SEM observations, yarn diameter around 3mm

SEM settings differ according to the thickness of the sample and the density of the fibers. Good quality images and a high magnification of the sample surfaces can be obtained. Furthermore, SEM is preferred as HMPE fibers are transparent which makes optical microscopy observations difficult.

1.2.2. Digital microscopy samples

Because of the transparency of the HMPE fibers, digital microscopy was not used for surface observations. However, it was used to observe the section of fibers, which were first cast in epoxy resin. To have a good image quality, the observation area of the sample has to be systematically polished from coarse to mirror finish (Figure 8.). Different samples were extracted from a 500kN break load braided rope

178 that experienced a hot bedding-in treatment during manufacture to stabilize its fiber assembly and
179 mechanical properties.
180 The observation of the 500kN braided rope was chosen as it included numerous lustered areas. The
181 section from a lustered textile axis made of Dyneema™ SK99 was examined to validate the observations
182 and the conclusions made for the Dyneema™ SK78 fibers extracted from the 500kN braided rope. A
183 disadvantage of the latter is that the level of the bedding-in load and the temperature history were
184 unknown.
185

Figure 8. Sample K cast in resin ready for digital microscope observations

186
187 1.2.3. Differential Scanning Calorimetry (DSC) samples
188
189 The crucibles of DSC analyzers are quite small. Two methods were used to place the fibers in the crucible,
190 depending on the kind of sample. If the fibers were not lustered, the strand was extracted. Then it was cut
191 into small pieces with a ceramic knife. If on the other hand the fibers were lustered, only the compacted
192 fibers from the upper surface were selected and placed in the crucible.
193
194 1.2.4. WAXS samples:
195
196 Wide Angle X-ray Scattering (WAXS) tests were performed at the Laboratory for Solid-state Physics at the
197 University of Paris-Sud. Strands were extracted from rope in different states. These samples were
198 positioned between two pieces of cardboard in order to be ready to put in the WAXS experimental set-
199 up (Figure 9.).

Figure 9. WAXS sample

Diffraction patterns were recorded with a MAR345 detector mounted on a rotating anode X-ray generator (copper anode, small focus, 40kV, 40mA). Multilayer optics are used to provide a monochromatic and parallel beam (wavelength 0.1542nm). Acquisition times were of the order of a few minutes.

2. Results

2.1. Visual and SEM observation

First, visual and SEM observations were made in order to understand this "lustering" phenomenon on coated and uncoated specimens.

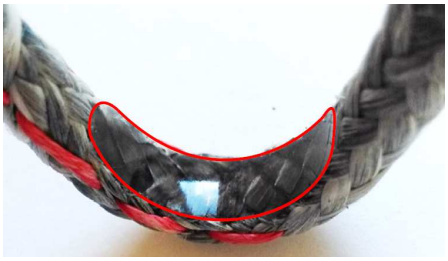

Figure 10. Visual observations of the contact surface between the textile axis and the ring of the pulley. The "lustered" area is outlined in red.

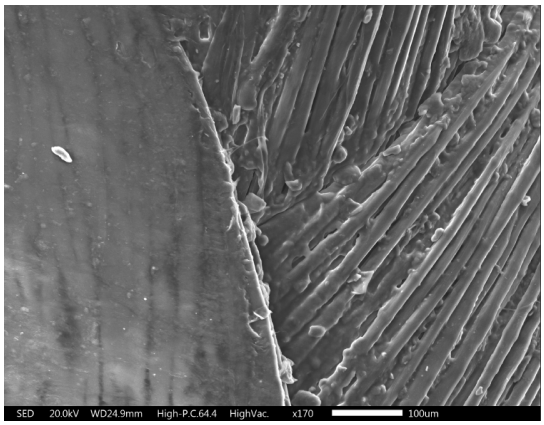

Figure 11. First SEM observations of lustered fibers (on the left side of the image).

213

Figure 12.a. Visual observations of sample B

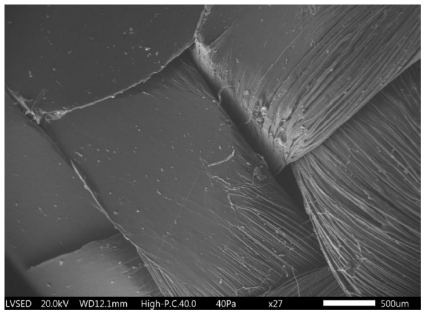

Figure 12.b. SEM observations of sample B

214

215 2.2. Digital microscope observations

216

217 Digital microscope observations were made on sub-strands extracted from the 500kN breaking load
218 braided rope described previously (Sample K, see Figure 2.a) and on strand from 4mm diameter rope
219 coming from the factory (Sample J, see Figure 2.b). The 500kN breaking load braided rope had
220 undergone a hot bedding-in. The yarn from this rope, similar to the HMPE rope loop of the pulley, had
221 been subjected to a complex mechanical loading with temperature rise, compression and tension loading.
222 The lustered areas of sample K are located in the strands. The 4mm diameter rope coming from the
223 factory had not been bedded-in. It can be considered that the filaments inside the sample J have not
224 been subjected to any previous mechanical loading. Following the experimental protocol described
225 earlier for SEM observations, Figure 13 and Figure 14 were obtained.

226

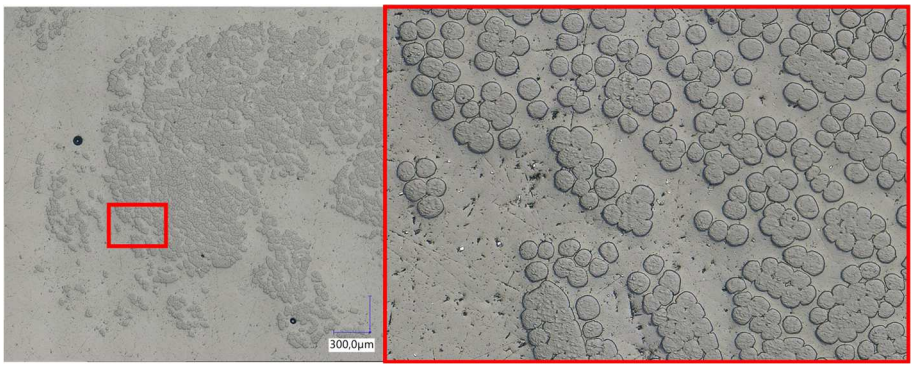

Figure 13. Digital microscope images of sample J

Figure 14. Digital microscope images of sample K

227

228 The section of a de-lustered area was observed with the digital microscope, cf Figure 15.

229

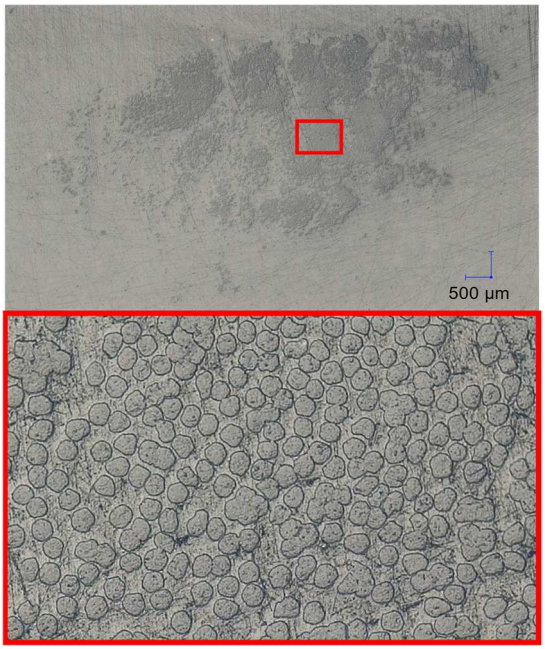

Figure 15. Digital microscope images of sample L after applying the de-lustering protocol.

230

231 After the de-lustering procedure, the fiber sections look very similar to their initial state. In order to
232 quantify the evolution of the fiber's diameter and section, digital microscope measurements were made
233 on several fiber sections (Figure 16.). Table 2. presents the results obtained.

234

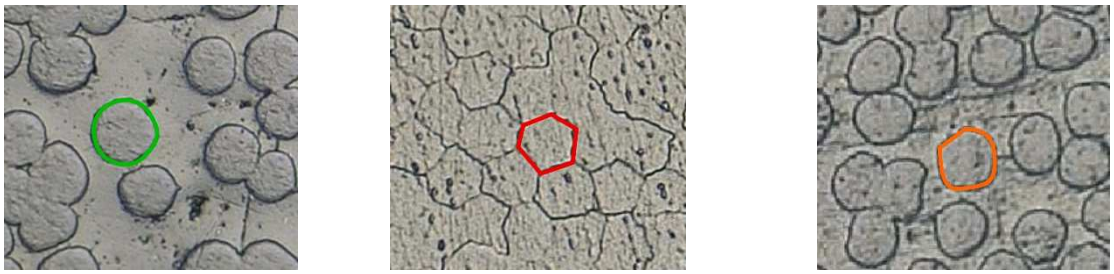

a. Initial state (Sample J) b. Lustered state (Sample K) c. De-lustered state (Sample L)

Figure 16. Evolution of the fiber sections for the different states

235

		Mean area in μm^2	Standard deviation on 10 measurements in μm^2	Mean equivalent diameter in μm
State	Initial	340	77.3	20.8
	Lustered	243	32.7	17.6
	De-lustered	313	49.7	20

Table 2. Mean areas of the fiber sections according to their state

236

237 2.3. DSC results

238

239 HMPE is known to be a fiber with a very high degree of crystallinity (greater than 90%). DSC (Differential
240 Scanning Calorimetry) measurements were performed for different HMPE fiber states. Figures 17 shows
241 the results for the different DSC samples. To refer to each sample, i is the number of the test.

242

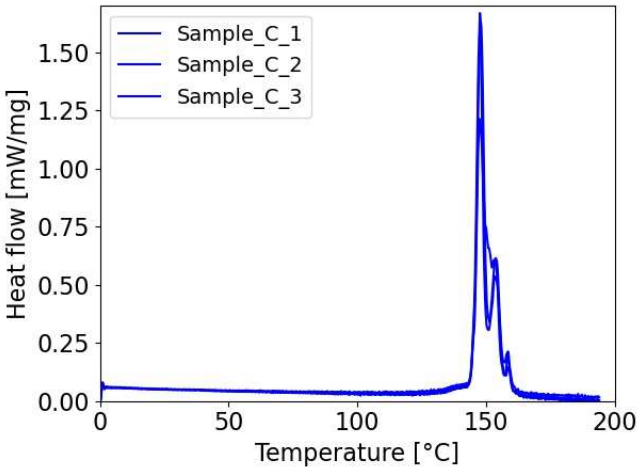

Figure 17.a. DSC results for samples D

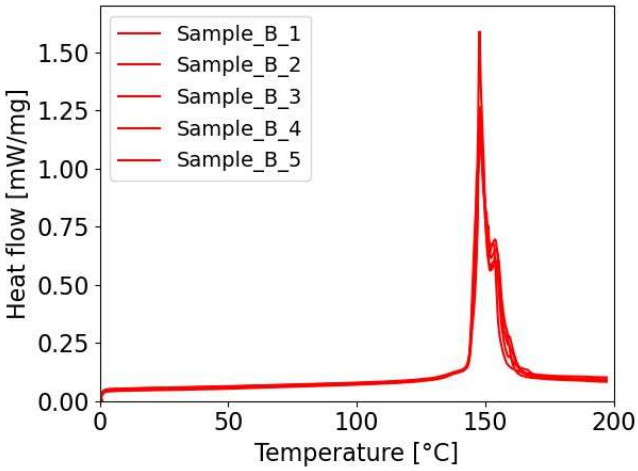

Figure 17.b. DSC results for samples C

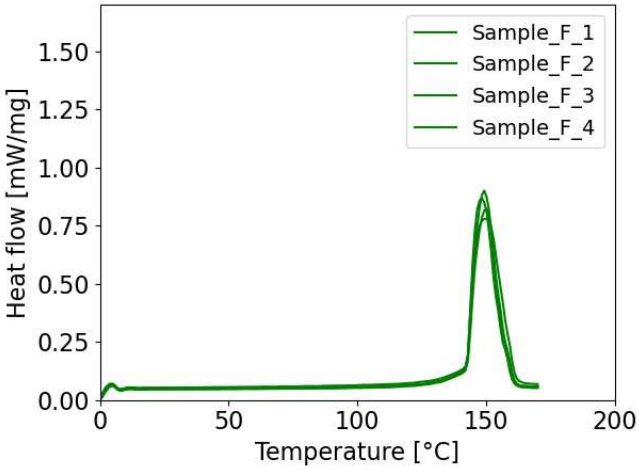

Figure 17.c. DSC results for samples G

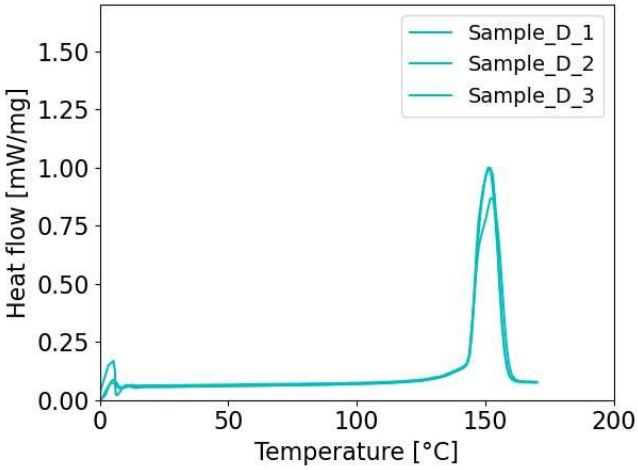

Figure 17.d. DSC results for samples E

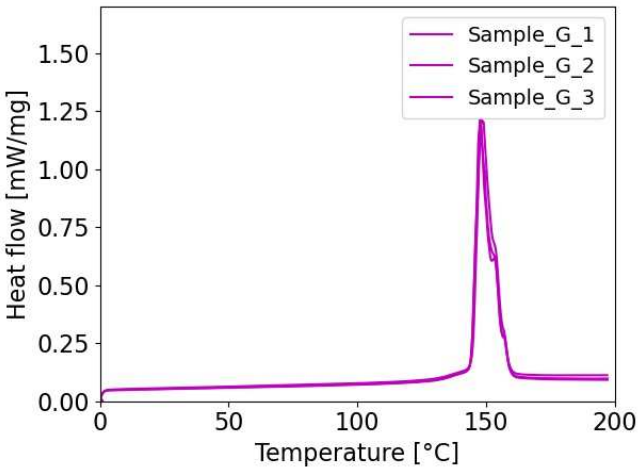

Figure 17.e. DSC results for samples H

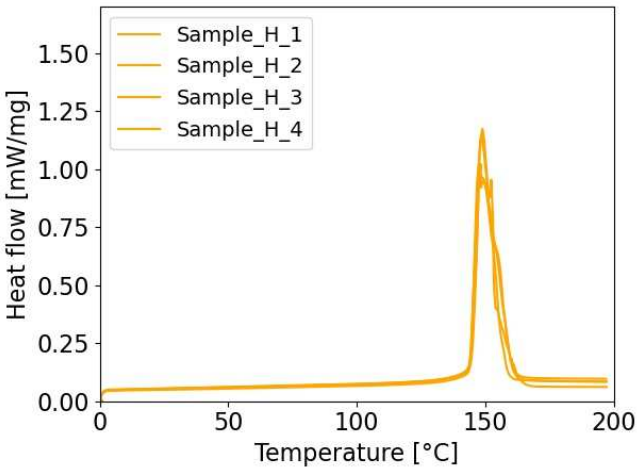

Figure 17.f. DSC results for samples I

243

244 2.4. WAXS results

245

246 WAXS (Wide Angle X-rays Scattering) was also performed for different HMPE fibers states. Figure 18
247 shows the results for the different WAXS samples.

248

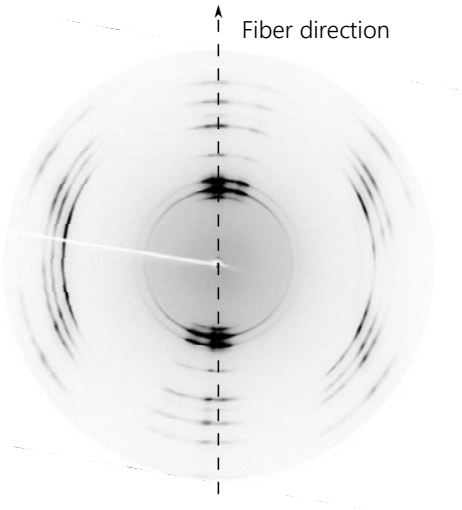

Figure 18.a. WAXS results for sample D

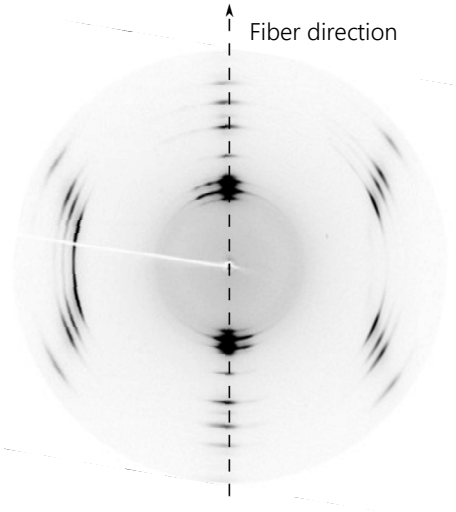

Figure 18.b. WAXS results for sample E

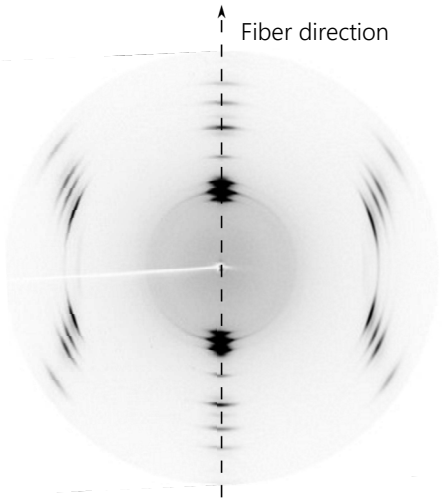

Figure 18.c. WAXS results for sample F

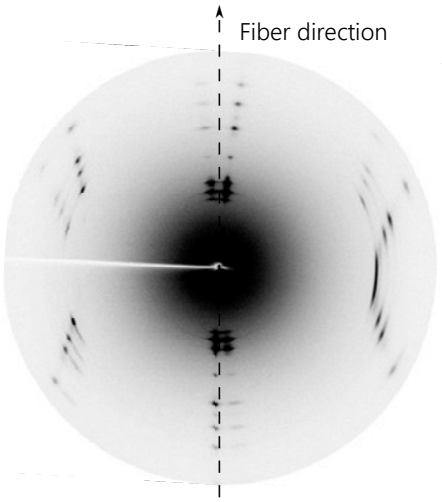

Figure 18.d. WAXS results for sample H

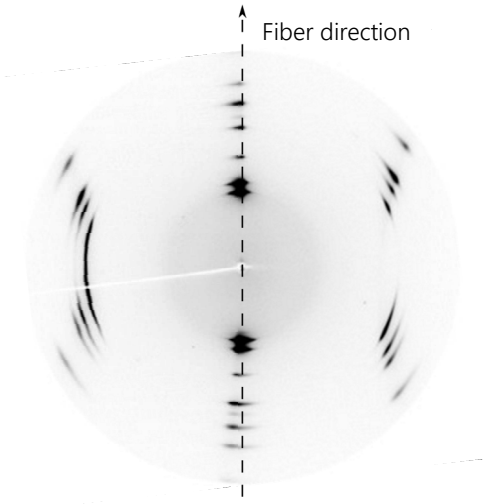

Figure 18.e. WAXS results for sample I

All these experimental results will now be discussed.

3. Discussion

First, visual and SEM observations were made in order to analyze this "lustering" phenomenon. As shown in Figure 10 and Figure 11, the lustered area can be characterized by several aspects such as:

- Darkening of the color and hardening of the contact area
- Optical reflectance for visual observations
- Difficulty to identify the individual fibers in the lustered area even with SEM observations.

SEM and digital microscope observations were used to examine three of the four hypotheses about the appearance of "lustering" on the contact surface of the HMPE loop: the migration of the coating, the compaction of the fibers, and the plasticity.

3.1. Migration of the coating

This first hypothesis was quickly checked by observing lustering on fibers without coating as shown on Figure 12.a and 12.b. Darkening of the surface is less evident but the optical reflectance and the hardening of the area were still identifiable. Also, on SEM images (Figure 12.b.) similar observations to those in Figure 8. can be made, where fibers are difficult to identify separately in lustered areas.

Thus, it can be concluded that the migration of the coating is not the cause of the lustering phenomenon. A coating may nevertheless be important in improving the abrasion resistance and affecting global friction between fibers and other materials. For the other hypotheses, more detailed observations were made.

3.2. Compaction

The observations of the cross sections of fibers with and without "lustering" on Figure 13 and Figure 14 are very interesting. The lustered sample shows smooth contours. The original circular sections of the fibers are highly compacted until reaching a prismatic "paving" shape, nearly hexagonal. Therefore, fibers tend to follow a spherical packing arrangement in which the fibers fill as much of the space as possible. It is difficult to distinguish fiber sections in the packing area; the fibers are deformed to fill the remaining space. Similar observations have already been made on wool fibers by Caldwell et al. (2005). This arrangement was also visible on observations of Dyneema™ SK76 fibers made by Bunsell (2018). Olley et al. (1993), Kabeel et al. (1994), Yan et al. (1997) for HMPE fibers and El-Maaty et al. (1996) for PP fibers, observed similar fiber arrangements produced by a hot compaction process.

The temperature reached by the pulley near the contact area is around 70 °C during a dynamic loading of 2kN (Bain, 2020). This is significantly lower than the temperature used for hot compaction process. If the compaction temperature is too low, there is insufficient melt to fill the interstices, the fibers deform into polygonal shapes, and insufficient transverse strength is developed (Kabeel et al., 1994). Nevertheless, some portion of HMPE fiber surfaces may melt at the contact area. Further investigations need to be carried out to observe interstitial material between HMPE fibers, in a similar way to the work of Olley et al. (1993).

297 3.3. Plasticity/ Permanent strain

298

299 Due to the heavy compaction that fibers undergo, the question of possible transverse plasticity/
300 permanent strain of the fibers can be posed. McDaniel et al. (2017) performed transverse compression
301 tests on Dyneema™ SK76 filaments with multiple load/unload cycles. The tests showed a non-linear
302 behavior with a stiffening under high strains. This increase in the stiffness can explain the apparent
303 hardening of the lustered area. During each unload, the filament does not return to its original diameter,
304 which indicates the presence of plasticity, cf Figure 19. However, the lustering phenomenon seems to be
305 reversible when a de-lustering protocol is used.

306

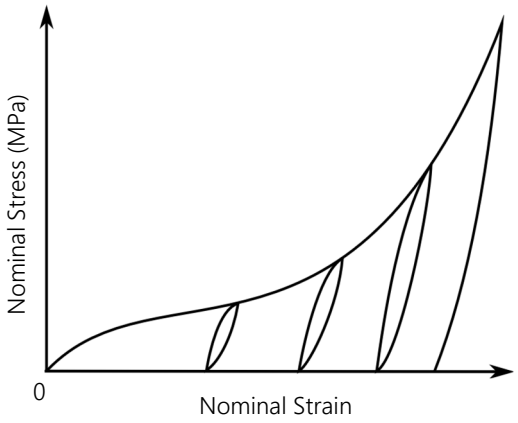

Figure 19. Mechanical response of HMPE filament with multiple char/discharge cycles on transverse compression (based on tests by McDaniel et al. (2017))

307

308 The evolution of the section of samples J, K and L can be observed and compared from Figure 17 and
309 Table 2, in order to characterize the transverse plasticity of HMPE filaments. After applying the de-
310 lustering protocol, the fibers seem to have returned to their initial state, cf Figure 13. The fibers undergo a
311 transverse deformation of around 28.5% between their initial state and the lustered state. These fibers
312 had a residual diametral strain of around 4% compared to their initial shape. This plasticity can be
313 explained by the fact that the filament is also itself an assembly but at a smaller scale. SEM observations
314 were made on the disassembly of a HMPE filament (Figure 20), and even smaller fibrillar elements, known
315 as fibrils, can be observed.

316

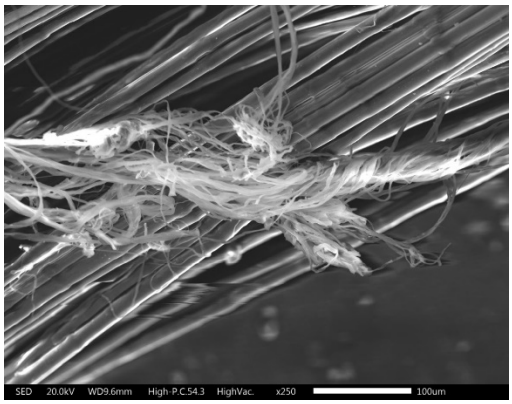

Figure 20. Disassembly of a HMPE filament

The filament is a complex structure of fibrils and voids. This suggests that there may be no plasticity within the fibrils but only suppression of the inter-fibril voids during contact, i.e. a change in the internal filament organization. The de-lustering protocol can make it possible to restore voids within and between the filaments.

An additional argument to rule out plasticity as a major factor of the analysis is to evaluate what would be the longitudinal strain induced by the radial strain observed, if plasticity was the main cause. In the case of pure plastic material, the volume is kept constant during the transformation, which leads to the relation:

$$\lambda_1 \lambda_2 \lambda_3 = 1$$

With:

- $\lambda_1 = L/L_0$ stretch in fiber direction with L deformed length and L_0 original length.
- $\lambda_2 \lambda_3 = (R/R_0)^2 = (\emptyset_{mean}/\emptyset_{init})^2 = (17.6/20.8)^2 = 0.716$ with λ_2 and λ_3 stretch in radial direction, R deformed radius, R_0 original radius, $\emptyset_{mean}$ mean equivalent diameter at de-lustered state and $\emptyset_{init}$ mean equivalent diameter at initial state.

Then for the case of constant volume strain, the elongation in the fiber direction is:

$$\lambda_1 = 1/0.716 = 1.40$$

This means that the induced axial deformation would be around 40%. However, the results obtained under monotonic tension tests show that the filament strain at break is around 4% (Figure 21). These two values therefore seem inconsistent and plasticity does not seem to be a key factor involved in the

lustering phenomenon. However, the high compaction and/or alignment of the fibrils within the filament does have a strong influence on the creation of this lustering phenomenon.

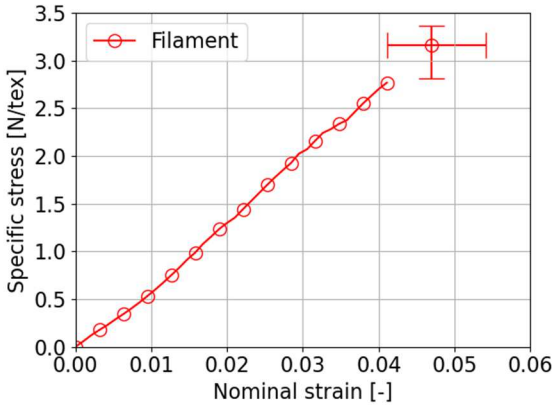

Figure 21. Monotonous axial tensile loading on filament of Dyneema™ SK99 (Mean behavior from 3 tests), Bain et al. (2020)

3.4. Modification of the microstructure

The final hypothesis to explain the lustering phenomenon is a modification of the microstructure of the HMPE fibers. HMPE is known to be a fiber with a very high degree of crystallinity (greater than 90%). In order to examine the hypothesis that this changes during lustering, DSC (Differential Scanning Calorimetry) measurements and WAXS (Wide Angle X-rays Scattering) were performed.

3.4.1. DSC analysis

The degree of crystallinity χ_c is defined by the ratio between the fusion enthalpy of the polymer ΔH_f and the theoretical fusion enthalpy of the 100% crystalline material ΔH_f^0:

$$\chi_c = \Delta H_f / \Delta H_f^0$$

3.4.1.1. Coating influence

Figure 17.a., Figure 17.b. and Table 3. show the results for the various measurements carried out on Dyneema™ SK99 coated (sample D) and uncoated (sample C).

Examining the heat flow curves as a function of temperature, we note that the trend is the same whether for coated or uncoated HMPE fibers. There is a main peak and two secondary peaks. The main peak characterizes the melting temperature of the main polymer chain. The melting temperatures are:

- $T_{fusion_D} = 147.6\,°C$ with a standard deviation of 0.12 °C from 3 tests
- $T_{fusion_C} = 147.9\,°C$ with a standard deviation of 0.06 °C from 5 tests

According to the manufacturer of these fibers, the melting point is between 144 °C and 152 °C. The temperatures obtained experimentally are within the range of the expected values.

With the mean values of fusion enthalpy obtained for HMPE fibers in sample C and B, and with a fusion enthalpy of 100% crystalline polyethylene $\Delta H^0_{f_{PE}}$ taken equal to 285 J/g. The degrees of crystallinity obtained are as follows:

- $\chi_{c_D} = 85.3\%$ with a standard deviation of 0.8% over 3 tests
- $\chi_{c_C} = 95.3\%$ with a standard deviation of 2.9% over 5 tests

There is a significant difference in the degrees of crystallinity of the two materials. This can be explained by the coating (C). As the latter contributes to sample weight but is not a material with a high degree of crystallinity, it reduces the apparent degree of crystallinity of Dyneema™ SK99.

Test number	Sample D	Sample C
1	242.0	280.4
2	241.5	273.5
3	245.6	277.8
4	/	261.7
5	/	264.6
Mean	**243.0 J/g**	**271.6 J/g**

Table 3. Fusion enthalpies in J/g for the two samples C (coated) and D (uncoated)

3.4.1.2. Lustering influence

Figure 17.c., Figure 17.d. and Table 4. show the results for the various measurements carried out on Dyneema™ SK99 fibers coated, not lustered, and extracted from a textile axis (Sample G) and Dyneema™

SK99 fibers coated, lustered and extracted from the same textile axis (Sample E). The samples were taken from an INO-BLOCK® pulley textile axis that underwent a dynamic loading. As a result, fibers had a complex mechanical loading together with heating. Extracting the two samples from the same loop reduces the influence of temperature on the results.

The heat flows for samples (G) and (E) are very similar. However, there is a change in the shape of the melting peaks compared to samples (D) and (C). This difference may indicate that changes have taken place in the crystalline phase of the material. The melting temperature are:

- $T_{fusion_G} = 151.9\,°C$ with a standard deviation of 0.36 °C for 3 tests
- $T_{fusion_E} = 149.3\,°C$ with a standard deviation of 0.83 °C for 4 tests

Test number	Sample G	Sample E
1	263.8	254.1
2	267.4	266.0
3	273.6	261.4
4	/	273.0
Mean	**268.3 J/g**	**263.6 J/g**

Table 4. Fusion enthalpies in J/g for the two states G (not lustered) and E (lustered)

The degrees of crystallinity obtained are as follows:

- $\chi_{c_G} = 94.1\%$ with a standard deviation of 2.78% over 3 tests
- $\chi_{c_E} = 92.5\%$ with a standard deviation of 2.79% over 4 tests

The crystallinity ratios obtained for the two materials are quite close but slightly higher for the lustered zone. The fiber used for the INO-BLOCK pulley loops is coated. If we compare the values of the crystallinity ratios obtained for samples G and E to the coated raw material from the factory (D); there is a notable difference. This increase in the rate of crystallinity of the HMPE loop can be explained by various factors. First, the complex mechanical loading can lead to reorientation of the fibers and crystallization (Tian and al., 2015). Second, the temperature rise on the pulley during loading can also induce the creation of crystals. This is why further analyses were carried out to understand the influence of mechanical loading and temperature.

Furthermore, in comparison to DSC results from Hine et al. (1993), no low-melting peak can be observed. It can be concluded that no significant portion of fibers has been melted. Indeed Hine et al. (1993) showed the appearance of a low-melting peak on the DSC melting endotherm when only 8% of fibers had been melted. So, either the melted fibers in the lustered cannot be measured through DSC or there are none. A morphological study could be performed to look at the regions between fibers in more detail.

3.4.1.3. Influence of Bedding-in and temperature

Figure 17.e., Figure 17.f. and Table 5. show the results for the various measurements carried out on the coated SK99 fibers with a bedding-in process at ambient temperature (Sample H) and Dyneema™ coated SK99 fibers with a bedding-in process at 100 °C (Sample I). The samples I were taken from a braid which had undergone a monotonic tensile test at a temperature of 100 °C without going to failure but which exceeded 20% nominal strain. The samples H were obtained from a braid which had undergone monotonous tension loading at room temperature until failure (nominal strain around 4%). This difference in deformation should be considered in the analyses. However, the goal here is not to quantify the contributions of temperature and mechanical loading on the increase in the degree of crystallinity. For this, additional analyses would be required.

The evolution of the heat flows for samples H and I are very similar. However, a change in the shape of the melting peaks can be noted, compared to the material D where 3 distinct peaks are observed. For samples H and I, these 3 peaks tend to form only one. In addition, using these curves, the melting temperature can be determined for the different materials:

- $T_{fusion_H} = 146.7\ °C$ with a standard deviation of 1.81 °C for 3 tests
- $T_{fusion_I} = 144.9\ °C$ with a standard deviation of 0.75 °C for 3 tests

Test number	Sample H	Sample I
1	251.1	277.9
2	252.3	264.2
3	264.7	269.0
Mean	**256.0 J/g**	**270.4 J/g**

Table 5. Fusion enthalpies in J/g for the two samples H and I

The degrees of crystallinity obtained were as follows:

- $\chi_{c_H} = 89.8\%$ with a standard deviation of 2.64% for 3 tests
- $\chi_{c_I} = 94.9\%$ with a standard deviation of 2.44% for 3 tests

The bedding-in at ambient temperature results in a 4.5% increase in the crystallinity ratio, while the bedding-in at 100 °C results in an increase of 9.5%. These increases are significant. The application of mechanical loading increases the degree of crystallinity within these fibers. Carrying out mechanical loading at a higher temperature facilitates the movement of molecular chains (Tian et al., 2015) and thus increases the degree of crystallinity for the bedding-in at 100 °C.

3.4.2. WAXS analysis

The analysis of 2D images from WAXS observations can be difficult to interpret for the untrained eye but the data obtained by X-ray diffraction are rich. Through measurements of the angle and the intensity of diffracted X-rays, it is possible to characterize the crystalline phase. For this study, the radial scan diffractogram is not analyzed. Only the diffraction pattern is used to characterize the microstructure of the fibers. Figure 22 illustrates the specific data of interest for this paper:

- the width "e" of a specific diffraction line is inversely related to the average dimension of crystallites along the considered direction: in other terms, the smaller the thickness "e", the larger this average dimension. This analysis is limited by the intrinsic resolution of the set-up that can be estimated using a powder made of macroscopic crystallites (typically quartz or silicon powders). In the present case, the width for all observed diffraction lines is resolution-limited that means that average crystallite dimensions are for all cases too large to be evaluated with the present set-up.

- the angular spread "Δα" of the azimuthal lines characterizes the orientation of the crystallites with respect to the fiber axis. The smaller the spread, the more the molecular chains are oriented in the average fiber direction. Care has to be taken that the observed angular spread is a convolution of the crystallite orientation within the individual fibers with the orientation of the individual fibers with respect to the average fiber direction.

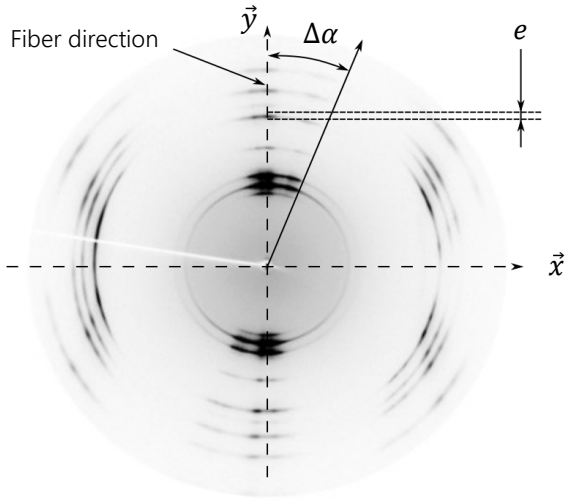

Figure 22. Data of interest on 2D image from WAXS observation

It would also be possible to analyze crystallinity ratio and crystal size based on these diffractograms, but that is not the aim here. It should be noted that during these measurements, the filaments making up the observed yarn are not perfectly aligned in the yarn direction. In addition, the network of chains that the X-rays must cross is complex. This explains the presence of other diffraction spots. For the case of a totally amorphous polymer material, a WAXS analysis would give a very diffuse ring of large thickness. For all the measurements performed, the presence of interrupted rings can be observed. This is characteristic of a crystal structure with a strong orientation of the crystallites in the fiber direction. We also note that the thickness of the rings is quite small, which confirms the presence of a material with a well-defined crystalline arrangement.

WAXS results on lustered fibers (see Figure 18.b and 18.c) show a slightly less diffuse ring with a smaller angle α than for the virgin fibers (see Figure 18.a.). The thickness e, is constant. These observations lead to the conclusion that lustering does not modify the crystal structure of HMPE fibers. The slight change in the crystal orientation in the fiber direction can be explained by the application of a tension on the fibers. To verify this hypothesis, two others samples were observed: sample H and sample I.

WAXS results from the bedded-in fibers at ambient temperature and at 100 °C (see Figure 18.d and 18.e), show a strong decrease in the alpha angle, especially for the case of bedding-in at ambient temperature. There is therefore a strong reorientation of the molecular chains in the direction of the fiber during bedding-in, that is not only affecting the rope construction. Another conclusion can be made from DSC measurements: sample H has a lower degree of crystallinity but the orientation distribution of the crystallites in the stretching axis seems to be stronger than for sample I. It seems that the higher temperature induces a higher crystallinity ratio but allows a faster relaxation of the crystals.

These WAXS analyses help to demonstrate the absence of change in microstructure between lustered HMPE fibers and HMPE fibers that experienced a similar tension mechanical loading without lustering (comparison between samples E and I). Indeed, the changes occurring in the microstructure of the lustered fibers are mainly explained by the mechanical loading applied to them when the pulley is tensioned. It has also been shown that it is still possible to improve the orientation of grade SK99 Dyneema™ fibers by applying a bedding-in (comparison between samples E and H). In order to optimize the bedding-in protocol of ropes, it would be interesting to perform fiber analyses at different controlled bedding-in levels and different temperatures, in order to analyze the evolution of the microstructure of the fibers during the process.

Conclusion

This paper investigates the lustering phenomenon observed in the contact area between textile ropes and a pulley ring. This phenomenon results in spectacular changes to the optical aspects of the contact area as well as greatly improving the friction performance of the pulley. The lustering phenomenon is often observed but is very poorly documented, and hardly reported for HMPE fibers. The complex thermomechanical loading on the loop seems to be the main cause of the appearance of the lustering phenomenon. Based on published literature on HMPE, several hypotheses are suggested to explain lustering; coating effects, fiber compaction, fiber plasticity or changes to the crystalline microstructure. Various samples have been studied, showing lustering or not, obtained under several mechanical loading and thermal conditions. First, SEM observations showed that the "lustering" phenomenon is visible on both coated and uncoated fibers, ruling out this hypothesis. Then, WAXS and DSC measurements showed that while the loading conditions can induce a change of crystallinity ratio and crystal orientation, these variations are related to the thermal and mechanical loading conditions but do not show any correlation to the fact that the samples were lustered or not. Finally, digital microscope observations of the cross section of fibers in the lustered area showed that fiber compaction is the main feature which is modified when lustering occurs. This compaction seems not to be induced by any fiber plasticity but rather by a rearrangement of the microfibrils. In conclusion, the high tension in the filaments of the loop as well as the flexure and compression applied by the pulley ring, the sliding of the ring relative to the loop, and the increase in the temperature lead to a specific arrangement of the filaments. This rearrangement leads to lustering and to the strong improvement of the friction properties. It is now possible to define lustering areas. However, it is difficult to quantitatively characterize the level of lustering that is achieved and hence, the optimal service or process parameters required to induce it. To do so, additional investigations

would be helpful, such as micro-indentation tests to characterize the hardness of the lustered fiber regions.

Acknowledgements

The authors would like to thank the French ANRT Agency (CIFRE n° 2016/1258) and INO-ROPE for their financial support.

547 References

548

549 Bain, C. (2020). *Compréhension et modélisation des mécanismes de contact des câbles en polyéthylène*
550 *haut module*. PhD thesis, ENSTA Bretagne.
551 Bain, C., Davies, P., Bles, G., Marco, Y., & Barnet, J. (2020). Influence of bedding-in on the tensile
552 performance of HMPE fiber ropes. *Ocean Engineering*, *203*.
553 https://doi.org/10.1016/j.oceaneng.2020.107144
554 Bunsell, A. (2018). *Handbook of Properties of Textile and Technical Fibers* Woodhead Publishing, ISBN:
555 9780081012727.
556 Caldwell, J. P., Mastronarde, D. N., Woods, J. L., & Bryson, W. G. (2005). The three-dimensional
557 arrangement of intermediate filaments in Romney wool cortical cells. *Journal of Structural Biology*,
558 *151*(3), 298–305. https://doi.org/10.1016/j.jsb.2005.07.002
559 El-Maaty, M. I. A., Bassett, D. C., Olley, R. H., Hine, P. J., & Ward, I. M. (1996). The hot compaction of
560 polypropylene fibres. *Journal of Materials Science*, *31*(5), 1157–1163.
561 https://doi.org/10.1007/bf00353094
562 Forster, A. L., Forster, A. M., Chin, J. W., Peng, J., Lin, C., Petit, S., Kang, K., Paulter, N., Riley, M. A., Rice, K.
563 D., & Al-sheikhly, M. (2015). *Long-term stability of UHMWPE fi bers*. *114*, 45–51.
564 https://doi.org/10.1016/j.polymdegradstab.2015.01.028
565 Golovin, K., & Phoenix, S. L. (2016). Effects of extreme transverse deformation on the strength of UHMWPE
566 single filaments for ballistic applications. *Journal of Materials Science*, *51*(17), 8075–8086.
567 https://doi.org/10.1007/s10853-016-0077-3
568 Hine, P. J., Ward, I. M., Olley, R. H., & Bassett, D. C. (1993). The hot compaction of high modulus melt-spun
569 polyethylene fibres. *Journal of Materials Science*, *28*(2), 316–324. https://doi.org/10.1007/BF00357801
570 Jiang, Z., Tang, Y., Men, Y., Enderle, H. F., Lilge, D., Roth, S. V, Gehrke, R., & Rieger, J. (2007). Structural
571 evolution of tensile-deformed high-density polyethylene during annealing: Scanning synchrotron
572 small-angle X-ray scattering study. *Macromolecules*, *40*(20), 7263–7269.
573 https://doi.org/10.1021/ma0627572
574 Jin, X., Wang, W., Bian, L., Xiao, C., Zheng, G., & Zhou, C. (2016). Improvement of coating durability ,
575 interfacial adhesion and compressive strength of UHMWPE fi ber / epoxy composites through
576 plasma pre-treatment and polypyrrole coating. *Composites Science and Technology*, *128*, 169–175.
577 https://doi.org/10.1016/j.compscitech.2016.03.026
578 Kabeel, M. A., Bassett, D. C., Olley, R. H., Hine, P. J., & Ward, I. M. (1994). Compaction of high-modulus
579 melt-spun polyethylene fibres at temperatures above and below the optimum. *Journal of Materials*
580 *Science*, *29*(18), 4694–4699. https://doi.org/10.1007/BF00356511
581 Litvinov, V. M., Xu, J., Melian, C., Demco, D. E., Möller, M., & Simmelink, J. (2011). Morphology, chain

582 dynamics, and domain sizes in highly drawn gel-spun ultrahigh molecular weight polyethylene
583 fibers at the final stages of drawing by SAXS, WAXS, and 1H Solid-State NMR. *Macromolecules*,
584 *44*(23), 9254–9266. https://doi.org/10.1021/ma201888f
585 McDaniel, P. B., Deitzel, J. M., & Gillespie, J. W. (2015). Structural hierarchy and surface morphology of
586 highly drawn ultra high molecular weight polyethylene fibers studied by atomic force microscopy
587 and wide angle X-ray diffraction. *Polymer*, *69*, 148–158. https://doi.org/10.1016/j.polymer.2015.05.010
588 McDaniel, P. B., Sockalingam, S., Deitzel, J. M., Gillespie, J. W., Keefe, M., Bogetti, T. A., Casem, D. T., &
589 Weerasooriya, T. (2017). Composites : Part A The effect of fiber meso / nanostructure on the
590 transverse compression response of ballistic fibers. *Composites Part A*, *94*, 133–145.
591 https://doi.org/10.1016/j.compositesa.2016.12.003
592 Morye, S. S., Hine, P. J., Duckett, R. A., Carr, D. J., & Ward, I. M. (1999). Comparison of the properties of hot
593 compacted gel-spun polyethylene fibre composites with conventional gel-spun polyethylene fibre
594 composites. *Composites Part A: Applied Science and Manufacturing*, *30*(5), 649–660.
595 https://doi.org/10.1016/S1359-835X(98)00175-4
596 Olley, R. H., Bassett, D. C., Hine, P. J., & Ward, I. M. (1993). Morphology of compacted polyethylene fibres.
597 *Journal of Materials Science*, *28*(4), 1107–1112. https://doi.org/10.1007/BF00400899
598 Sockalingam, S., Casem, D., Weerasooriya, T., McDaniel, P., & Gillespie, J. (2017). Experimental
599 Investigation of the High Strain Rate Transverse Compression Behavior of Ballistic Single Fibers.
600 *Journal of Dynamic Behavior of Materials*, *3*(3), 474–484. https://doi.org/10.1007/s40870-017-0126-2
601 Tang, Y., Jiang, Z., Men, Y., An, L., Enderle, H. F., Lilge, D., Roth, S. V., Gehrke, R., & Rieger, J. (2007).
602 Uniaxial deformation of overstretched polyethylene: In-situ synchrotron small angle X-ray scattering
603 study. *Polymer*, *48*(17), 5125–5132. https://doi.org/10.1016/j.polymer.2007.06.056
604 Tian, Y., Zhu, C., Gong, J., Ma, J., & Xu, J. (2015). Transition from shish-kebab to fibrillar crystals during
605 ultra-high hot stretching of ultra-high molecular weight polyethylene fibers : In situ small and wide
606 angle X-ray scattering studies. *European Polymer Journal*, *73*, 127–136.
607 https://doi.org/10.1016/j.eurpolymj.2015.10.006
608 Vlasblom, M. (2018). 18 - The manufacture, properties, and applications of high-strength, high-modulus
609 polyethylene fibers. In *Handbook of Properties of Textile and Technical Fibres*. Elsevier Ltd.
610 https://doi.org/10.1016/B978-0-08-101272-7.00018-3
611 Yan, R. J., Hine, P. J., Ward, I. M., Olley, R. H., & Bassett, D. C. (1997). The hot compaction of SPECTRA gel-
612 spun polyethylene fibre. *Journal of Materials Science*, *32*(18), 4821–4832.
613 https://doi.org/10.1023/a:1018647401619
614
615